Journal of Materials Chemistry C

ROYAL SOCIETY OF CHEMISTRY

PAPER

View Article Online
View Journal

Cite this: DOI: 10.1039/d5tc03740a

Zwitterion-assisted growth and strain optimisation of perovskite single crystals for high-performance photon counting radiation detection

Jayana Jayarathne, [a] Joydip Ghosh, [ab] Justin Reiss, [c] Robert Lavelle, [cd] Steven J. Hinder, [e] Douglas Wolfe, [d] Carol Crean [f] and Paul Sellin *[a]

Received 17th October 2025,
Accepted 10th February 2026

DOI: 10.1039/d5tc03740a

rsc.li/materials-c

Solution-grown perovskite single crystals (SCs) have attracted great interest in the radiation detection community due to their easier growth process and cost-effectiveness compared to conventional semiconductor materials such as cadmium telluride (CdTe) and cadmium zinc telluride (CdZnTe), as well as melt-grown perovskite materials such as $CsPbBr_3$ (CPB). However, their performance as photon-counting radiation detectors is inferior to that of melt-grown semiconductor materials. This is due to the potential of the solution-growth method to cause unregulated crystal growth and poor scalability of high-quality SCs due to spontaneous nucleation. In this work, using the sulfonic zwitterionic ligand 3-(decyldimethylammonio)propanesulfonate inner salt (DPSI), we have grown high-quality $FAPbBr_3$ (FPB) SCs with low defect densities. Also, by optimising the crystal growth temperature ramp, we have obtained 'low-strained' FPB SCs with reduced internal strain. These SC devices show excellent charge transport properties, showing a high hole mobility of 190 $cm^2\ V^{-1}\ s^{-1}$ and a high hole mobility–lifetime ($\mu\tau$) product of $2.7 \times 10^{-3}\ cm^2\ V^{-1}$, with a low dark current of 2.9 nA cm^{-2} at a field strength of 1000 V cm^{-1}. These devices have achieved an energy resolution of 10.5% FWHM for ^{241}Am 5.49 MeV α-particles and 25.6% FWHM for ^{241}Am 59.5 keV γ-rays, and a high X-ray photocurrent sensitivity of 5111 μC $Gy_{air}^{-1}\ cm^{-2}$ for 50 kV X-rays, showing great promise as room-temperature radiation detectors capable of operating efficiently in both photon-counting and current modes.

1. Introduction

High-energy radiation detection plays a pivotal role in medical diagnostics, nuclear security and scientific research. Various semiconductor materials have been utilised for direct radiation detection, including cadmium telluride (CdTe), cadmium zinc telluride (CdZnTe, CZT), amorphous selenium (a-Se) and high-purity germanium (HPGe).[1–3] These commercialised semiconductor radiation detectors operate efficiently in both current and pulse detection modes; for instance, CZT has achieved an X-ray sensitivity of 2400 μC $Gy_{air}^{-1}\ cm^{-2}$ for 80 kVp X-rays in the photocurrent mode, while achieving <1% energy resolution for 662 keV ^{137}Cs γ-rays in the photon counting mode.[4,5] However, while these semiconductors have achieved excellent performance as radiation detectors, the high cost and production difficulty have motivated the direct radiation detector community to search for alternative high-atomic-number (Z) semiconductor materials.

Metal halide perovskites have become popular materials for radiation detection due to their high Z composition, excellent optoelectronic properties and low production cost.[6] Of particular interest are metal halide perovskites with the structure ABX_3, where A is an organic or inorganic cation (Cs^+, MA^+ (CH_3NH_3), FA^+ ($CH(NH_2)_2$)), B is a metal cation (Pb^{2+}, Sn^{2+}) and X is a halogen anion (Cl^-, Br^-, I^-).[6] These materials have demonstrated excellent performance as radiation detectors; for example, $CsPbBr_3$ (CPB) single crystals (SCs), which can be synthesised through melt-grown synthesis methods like the Bridgman–Stockbarger method, have shown a 1.4% energy resolution for 662 keV ^{137}Cs γ-rays.[7] However, as with the production of CZT, the synthesis of melt-grown perovskites requires high temperature and is therefore highly energy-intensive. In addition, the phase transitions of CPB that occur due to the cooling of the crystals to room temperature during the growth process (cubic–tetragonal at 130 °C and

[a] School of Mathematics and Physics, University of Surrey, Guildford, GU2 7XH, Surrey, UK. E-mail: p.sellin@surrey.ac.uk
[b] Inorganic Chemistry Laboratory, University of Oxford, Oxford, OX1 3QR, UK
[c] Applied Research Laboratory, The Pennsylvania State University, USA
[d] Materials Science and Engineering, The Pennsylvania State University, USA
[e] School of Mechanical Engineering Sciences, University of Surrey, Guildford, GU2 7XH, UK
[f] School of Chemistry and Chemical Engineering, University of Surrey, Guildford, GU2 7XH, UK

tetragonal–orthorhombic at 88 °C) induce cracking of CPB SCs due to thermomechanical strain.[7,8]

Therefore, solution-grown hybrid perovskites, particularly $FAPbBr_3$ (FPB), have gained significant attention due to their low-temperature growth process and lower production cost. These materials remain in the cubic phase during the crystallisation process and do not show phase transitions around room temperature, mitigating phase transition-induced strain during growth.[9] Nevertheless, reproducible growth of FPB SCs remains a key challenge due to the uncontrolled nucleation and rapid crystallisation, which often leads to the formation of polycrystals and non-uniform morphologies.[9,10]

In addition to the challenges in the synthesis of high-quality and scalable perovskite SCs, including FPB as mentioned above, various structural imperfections within the crystal lattice hinder the optoelectronic performance. Among these, bulk strain has been shown to be a critical factor affecting the performance of perovskites. Bulk strain can originate from various factors such as the thermal strain and lattice distortions during the growth of these SCs.[10,11] Previous reports have established a correlation between the bulk strain and the device performance of perovskite monocrystalline X-ray detectors.[12] Despite this understanding, the effect of strain on perovskite photon counting α-particle and γ-ray radiation detectors remains predominantly unexplored, particularly how strain influences the material's charge transport properties. Addressing this gap is crucial for the advancement and future commercialisation of perovskite SC photon counting detectors.

In this work, we have grown FPB SCs using a modified inverse temperature crystallisation (ITC) method, which involves seeded solution growth as shown in Fig. 1a. In order to control the growth dynamics, we have used a sulfonic

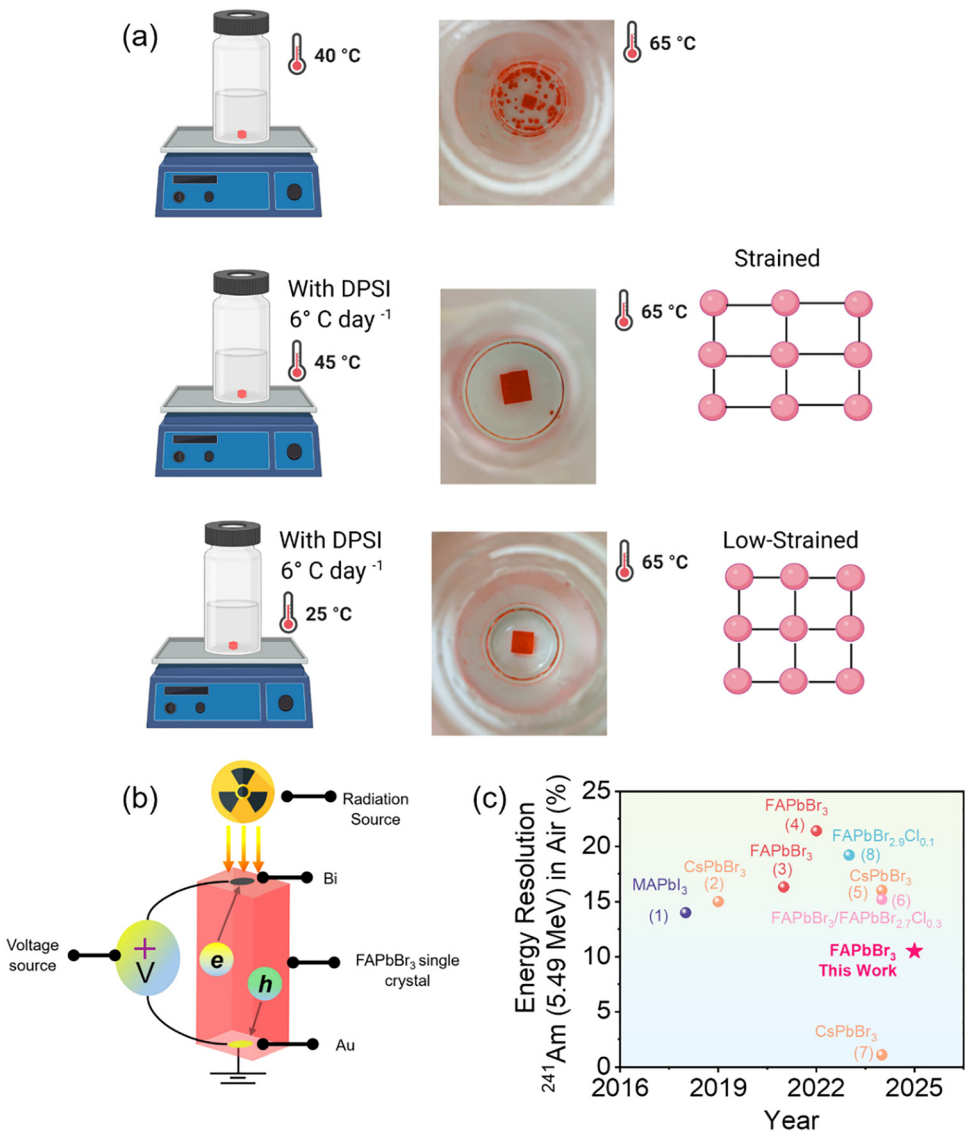

Fig. 1 (a) A schematic diagram of the crystal growth setup. (b) The overall FPB SC device structure. (c) The current performance of perovskite single crystal α-particle detectors operating under ambient conditions: (1) $MAPbI_3$,[42] (2) $CsPbBr_3$,[35] (3) $FAPbBr_3$,[9] (4) $FAPbBr_3$,[43] (5) $CsPbBr_3$,[44] (6) $FAPbBr_3$/$FAPbBr_{2.7}Cl_{0.3}$,[45] (7) $CsPbBr_3$,[46] and (8) $FAPbBr_{2.9}Cl_{0.1}$.[47]

zwitterionic ligand, 3-(decyldimethylammonio)propanesulfonate inner salt (DPSI). DPSI has previously been used to grow other perovskite materials, enabling a significant reduction in spontaneous nucleation in $MAPbBr_3$ (MPB).[13–15] By utilising a slow linear temperature ramp, we have grown well-formed FPB SCs without the formation of multiple nuclei and polycrystals. Additionally, by modifying the growth temperature ramp, we demonstrate the reduction of internal strain in the single crystals. We utilised an asymmetric contact structure as shown in Fig. 1b, which aided in the suppression and stabilisation of dark currents due to blocking of charge injection[8] (see Note S1 and Fig. S1, SI).

Through these optimisations, we improved the charge transport properties of the FPB SCs and achieved a hole mobility of 190 $cm^2\ V^{-1}\ s^{-1}$, and a hole mobility–lifetime product of $2.7 \times 10^{-3}\ cm^{-2}\ V^{-1}$. This was reflected in the performance of these low-strained FPB SCs as spectroscopic α-particle and low-energy gamma-ray detectors, which resulted in an energy resolution of 10.5% for ^{241}Am 5.49 MeV α-particles as shown in Fig. 1c.

2. Experimental section

2.1 Materials

Formamidinium bromide (FABr) (>99.99%) was purchased from GreatCell Solar Materials. Lead(II) bromide ($PbBr_2$) (≥98%), DPSI, *N*,*N*-dimethylformamide (DMF, 99.8%), and γ-butyrolactone (GBL, >99.9%) were purchased from Sigma-Aldrich. All materials were used as supplied without further purification.

2.2 Growth of $FAPbBr_3$ single crystals

A 1.4 M FPB precursor solution was prepared by dissolving FABr and $PbBr_2$ in a mixture of DMF and GBL (1 : 1 v/v). The precursor solution was then stirred and sonicated to achieve complete dissolution. The solution was then filtered using a 0.22 μm pore size polyvinylidene fluoride (PVDF) filter membrane. A 10% molar concentration of DPSI (1.40 mmol) was then added to the precursor solution and then further sonicated. A small seed crystal was added to the filtered precursor solution contained in a glass vial, which was placed in a silicone oil bath on a hot plate with a starting temperature of 45 °C. The perovskite solution was heated using a slow heat ramp of 6 °C day^{-1} for seeded FPB SC growth. To obtain low-strained FPB SCs, the temperature ramp was initiated at room temperature and then increased to 47 °C in 3 hours. Afterwards, the ramp proceeded at a rate of 6 °C day^{-1}. The crystals were then extracted at 65 °C for growing both strained and low-strained FPB SCs. After the crystals were extracted, they were washed using toluene to remove precursor residues and stored in a nitrogen atmosphere for further processing.

2.3 Detector fabrication

As-grown FPB SCs were manually polished using Al_2O_3 powder with different grain sizes and 2-propanol (IPA) as the polishing lubricant. Bi/FPB SC/Au devices were fabricated by thermally evaporating an 80 nm layer of Bi on the top surface and an 80 nm layer of Au on the bottom surface of the SCs (Edwards 306A, Edwards Vacuum, UK). For trap density measurements, an 80 nm layer of Au was deposited on the top and bottom surfaces of the SCs. For γ-ray spectroscopic radiation detection measurements, a guard ring electrode structure was fabricated using a mechanical mask.

2.4 Characterisation techniques

Photoluminescence measurements. Steady-state photoluminescence measurements were performed using a 405 nm laser and an Ocean Optics Maya 2000 spectrometer. Time-resolved photoluminescence measurements were conducted using a pulsed PicoQuant (LDH-405) laser with an excitation wavelength of 405 nm and 50 ps pulse width.

Current–voltage characterisation. Current–voltage (*I–V*) characterisation was performed using a Keithley 487 picoammeter/voltage source.

X-ray diffraction measurements. The crystals were characterised by high-resolution X-ray diffraction (HRXRD) using a Malvern Panalytical X'Pert3 Materials Research Diffractometer (MRD) XL system with a Cu $K\alpha_1$ radiation source (λ = 0.154 nm). Double-axis and triple-axis symmetric (100) X-ray rocking curves (XRRCs) were collected in point-focus mode using a 4× Ge (220) hybrid monochromator. $FAPbBr_3$ has a cubic crystal structure with lattice constants a, b, and c = 5.9961 Å, and the (100) reflection corresponds to a 2θ value of 14.7619°.[16] A PIXcel detector was used in the double-axis setup and a Xe proportional detector was used for the triple-axis scans. With the triple-axis setup, scans were collected along both the ω and ω:2θ scanning axes to assist with decoupling contributions to peak broadening from lattice tilt and lattice strain.[17,18]

Raman spectroscopic measurements. Raman spectroscopy was performed using a Renishaw inVia confocal Raman microscope. The following conditions were used for the Raman mapping: a 633 nm laser (20 mW total power) fitted with a cross-polarising filter in the *Z*(*X*, *Y*)*Z* configuration using 5% laser power at the sample. Spectra (60–1250 cm^{-1}) were recorded at 50 micron steps across the entire surface of the crystal. Raman images were generated by comparing the signal to baseline intensities in the spectral region of 80–250 cm^{-1}.

Fourier transform infrared spectroscopy measurements. Infrared (IR) spectroscopy was carried out on a PerkinElmer Spectrum Two FT-IR spectrometer with a diamond ATR crystal. Spectra were measured between 4000 and 400 cm^{-1} with a 4 cm^{-1} resolution.

For sample preparation, 0.8 M solutions of DPSI mixed with FABr in DMF and DPSI mixed with $PbBr_2$ in DMF were dried using a rotary evaporator to obtain solid residues for analysis.

X-ray photoelectron spectroscopy measurements. X-ray photoelectron spectroscopy (XPS) analyses were performed on a Thermo Fisher Scientific (East Grinstead, UK) K-Alpha+ spectrometer. XPS spectra were acquired using a monochromated Al Kα X-ray source (hn = 1486.6 eV). An X-ray spot with a ~400 μm radius was employed. Survey spectra were acquired using a pass energy of 200 eV. High-resolution core-level spectra for all elements were

acquired with a pass energy of 50 eV. All high-resolution core-level spectra were charge-referenced against the C 1s peak at 285 eV to correct for charging effects during acquisition. Quantitative surface chemical analyses were conducted using the high-resolution core-level spectra following the removal of a non-linear (Shirley) background. The Avantage software was used, which incorporates the appropriate sensitivity factors and corrects for the electron energy analyser transmission function.

Radiation detection characterisation. For X-ray photocurrent and sensitivity measurements, FPB SC detectors were irradiated using an Amptek Mini X2 (Amptek, Bedford) X-ray tube with an accelerating voltage of 50 kV and a maximum tube current of 200 μA. The X-ray air kerma dose rate was calibrated using an IBA FC65-G 0.65 cm^3 gas ionization chamber. α-Spectroscopic measurements were carried out using an Amptek PX4 Digital Pulse Processor with a peaking time of 32 μs (equivalent analogue shaping time of 14.5 μs) and an Ortec 710 HV power supply. For analogue pulse height measurements, an Ortec Easy-MCA 8k multi-channel analyser and an Ortec 572 shaping amplifier were used. A ^{241}Am 5.49 MeV uncollimated α-particle source with an activity of 5 kBq was used for α-particle spectroscopic measurements. For gamma-ray spectroscopic measurements, an uncollimated ^{241}Am 59.5 keV γ-ray source with an activity of 400 kBq was used. Prebiasing was not applied for radiation detection measurements carried out in this work.

Drift mobility calculations. Drift mobility was measured using alpha particle time of flight (TOF). ^{241}Am 5.49 MeV α-particle pulses from the charge sensitive preamplifier were captured using a Tektronix TDS 2024C four-channel digital storage oscilloscope and recorded for off-line analysis. 500 pulses were recorded at each bias voltage and the charge drift time was measured from the 10–90% rise time for each pulse. The limiting rise time of the Ortec 142A preamplifier was ~2 ns. Due to the low penetration depth of α-particles on FPB SCs, the alpha-particle TOF measures the single-carrier drift mobility of either holes or electrons depending on the bias polarity. The mean charge drift time t_{dr} is determined for each applied electric field and the drift mobility is calculated using

$$\mu = \frac{V_{dr}}{E} = \frac{d^2}{V \times t_{dr}} \quad (1)$$

where μ is the mobility, V_{dr} is the drift velocity, E is the applied electric field, d is the thickness of the detector, and V is the applied voltage.

3. Results and discussion

3.1 Zwitterion-assisted growth of $FAPbBr_3$ single crystals

The DPSI zwitterion comprises a quaternary ammonium group, a sulfonate group and a long alkyl chain,[19] as shown in Fig. 2a. We hypothesised that the sulfonate group of the DPSI interacts with the Pb^{2+} and FA^+ ions of the perovskite at the perovskite/solution interface. These interactions and the steric hindrance effect caused by the long alkyl chain of the zwitterionic molecule substantially slow down the nucleation kinetics of the FPB SC growth, thereby enabling a more controlled crystal growth process. To verify this hypothesis, we conducted Fourier transform infrared spectroscopy (FTIR) measurements on dried powders of DPSI, FABr mixed with DPSI, and $PbBr_2$ mixed with DPSI, as shown in Fig. 2b and c. The IR spectrum of the DPSI zwitterionic molecule consists of two characteristic vibrational features at 1030 cm^{-1} and 1038 cm^{-1}.[14] These correspond to the symmetric stretching modes of the sulfonate ($-SO_3^-$) group of the zwitterionic molecule. Upon mixing $PbBr_2$ with the DPSI,

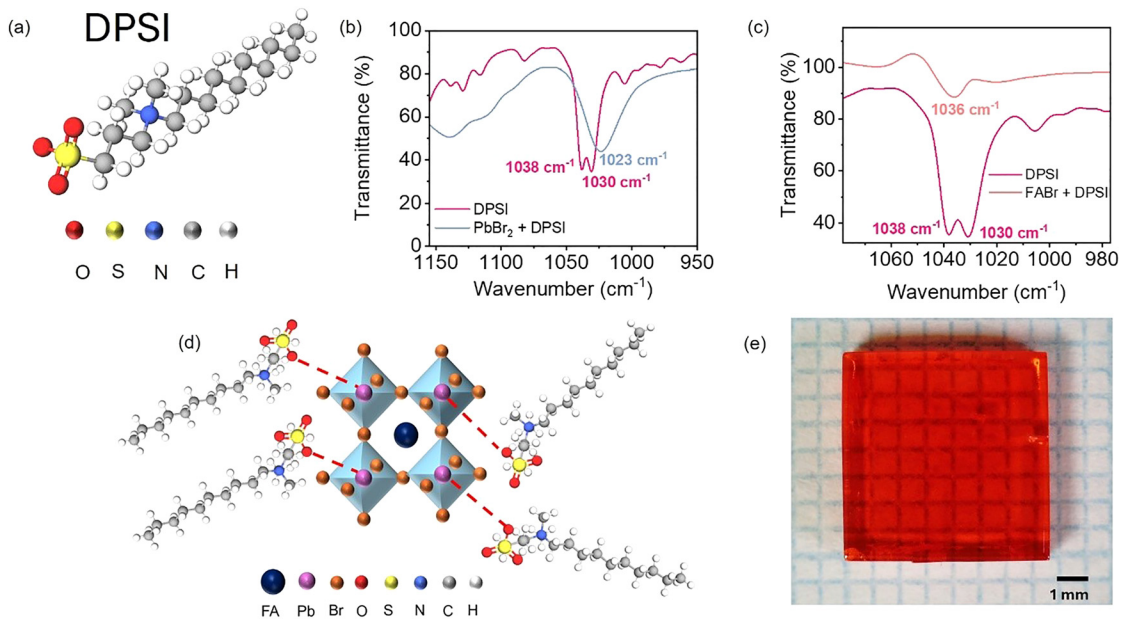

Fig. 2 (a) Molecular structure of the DPSI zwitterion. (b) FTIR spectra of DPSI and DPSI mixed with $PbBr_2$. (c) FTIR spectra of DPSI and DPSI mixed with FABr. (d) The crystal structure of the FPB perovskite and the interaction of the DPSI with the perovskite. (e) A polished FPB SC grown with the DPSI additive.

we observe that the sulfonate peak centred around 1030 cm^{-1} broadens and shifts to lower wavenumbers, with the peak centred at 1024 cm^{-1}. This shows that the sulfonate group of the DPSI interacts with the Pb^{2+} ions of the perovskite. Upon the addition of FABr to DPSI, the $-SO_3^-$ symmetric vibrations of the DPSI undergo a slight redshift and peak broadening with a new peak centred around 1036 cm^{-1}. This is attributed to the hydrogen bonding of the N–H group of the FA^+ ions with the sulfonic group of the DPSI.[20] Such interactions suggest that DPSI can interact with both uncoordinated Pb^{2+} ions and FA^+ ions of the perovskite during the solution growth process.[14,20]

We believe that the DPSI molecule transiently interacts with the perovskite/solution interface of the emerging nucleus during the growth process, with the long alkyl chain protruding outwards as shown in Fig. 2d. This long alkyl chain creates a steric hindrance effect, which hinders the accelerated ionic diffusion to the crystal surface, reducing the rapid attachment of ions and regulating the local supersaturation of the perovskite solution.[14] This regulates and slows the crystal growth rate and suppresses spontaneous nucleation, allowing us to obtain large-area FPB SCs with average dimensions of $7 \times 7 \times 3$ mm^3, as shown in Fig. 2e.

While the role of DPSI in regulating the crystal growth process is clear, we also investigated whether DPSI is incorporated into the FPB SC lattice. We conducted X-ray photoelectron spectroscopy (XPS) measurements on FPB SCs grown with DPSI. We exposed the bulk of the FPB SC by polishing the surface of the as-grown SC. The binding energy region related to S 2p did not show any distinctive peaks, as shown in Fig. S2. This indicates that sulphur features are absent from the crystal surface of a polished DPSI-based FPB SC. Therefore, the absence of signatures of DPSI in the polished DPSI-based single crystal suggests that DPSI only acts as a growth regulation ligand at the perovskite nucleus/solution interface and does not attach to the FPB SC lattice as a bulk passivating agent.

We subsequently carried out optical and electrical measurements to evaluate the performance of FPB SCs grown with the assistance of DPSI. Steady-state photoluminescence (PL) measurements (Fig. 3a) show that both pristine and DPSI-assisted FPB SCs exhibit an emission peak centred at 555 nm. Notably, the PL intensity is substantially higher in the DPSI-based FPB SC compared to its pristine counterpart. The average time-resolved PL (TRPL) lifetimes are shown in Fig. 3b, which were calculated using the following equation:[22]

$$\tau_{avg} = \frac{(A_1\tau_1^2) + (A_2\tau_2^2)}{(A_1\tau_1) + (A_2\tau_2)} \quad (2)$$

The SC grown with DPSI shows a significantly longer average PL lifetime of 159 ± 6 ns compared to the 98 ± 5 ns decay lifetime obtained for the pristine crystal. Both steady-state PL and TRPL measurements suggest a reduction in the concentration of non-radiative recombination centres in the DPSI-based FPB SC. This is attributed to the zwitterion-mediated

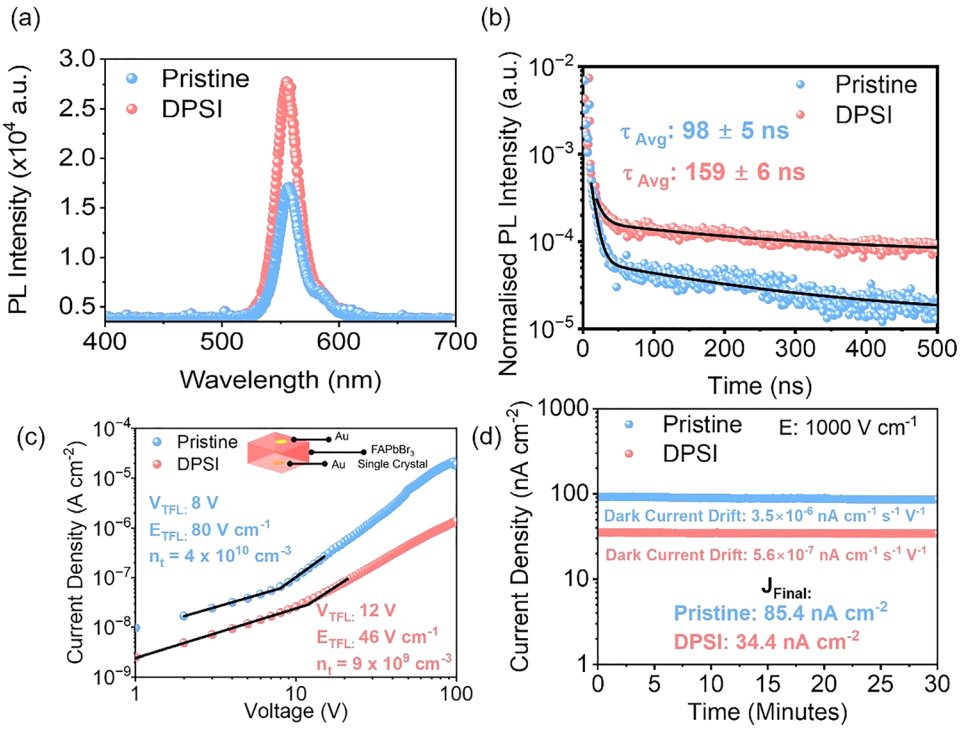

Fig. 3 (a) Steady-state photoluminescence behaviour of the pristine and DPSI-based perovskite SCs. (b) Time-resolved photoluminescence behaviour of the pristine SC and the SC grown with DPSI. (c) Trap density of the pristine and DPSI-based SCs obtained through SCLC measurements. The thickness of the pristine SC was 1 mm and the thickness of the DPSI SC was 2.6 mm. E_{TFL} is the trap filled electric field strength. (d) Temporal dark current behaviour of the pristine and DPSI-based SCs.

regulation of crystal growth, which suppresses trap formation in the perovskite material.[14]

Space charge limited current (SCLC) measurements were carried out to determine the trap density of our FPB SCs, as shown in Fig. 3c. Trap density is a critical parameter influencing the overall charge transport efficiency of perovskite-based radiation detectors; elevated defect densities potentially reduce carrier mobility and limit carrier lifetimes, reducing the device performance.[21] The trap densities for both pristine and DPSI-based FPB SCs were extracted using the SCLC model based on the following relation:[22]

$$V_{\mathrm{TFL}} = \frac{q n_{\mathrm{t}} L^2}{2\varepsilon} \quad (3)$$

where V_{TFL} is the trap-filled voltage, q is the elementary charge, n_{t} is the trap density, L is the thickness of the detector and ε is the dielectric constant of the perovskite, with FPB having a dielectric constant of 43.6.[23] As shown in Fig. 3c, the trap density of the DPSI-based device was calculated to be 9×10^9 cm^{-3}. This is a fourfold reduction compared to the pristine SC device, which exhibited a trap density of 4×10^{10} cm^{-3}. We attribute this reduction in trap density to the regulation of the crystal growth kinetics resulting from the interactions of the DPSI with the perovskite and the steric hindrance effect caused by the long alkyl chain, which significantly regulates the crystal growth process and thus reduces the formation of point defects in the bulk of the single crystal.

Previous reports have shown that the reduced defect density of perovskite SCs tends to support a low and stable dark current due to the reduction of ion migration.[14] In order to verify this, we conducted temporal dark current measurements of pristine and DPSI-based devices, as shown in Fig. 3d. The current drift was calculated using the following equation:[24]

$$D = \frac{(J_{\mathrm{initial}} - J_{\mathrm{Final}})}{Et} \quad (4)$$

where D is the current drift, J_{initial} and J_{final} are the initial and final current densities, E is the electric field strength, and t is the duration.

As shown in Fig. 3d, the DPSI-based device showed a dark current density of $\sim$34 nA cm^{-2} and the pristine device showed a dark current density of $\sim$84 nA cm^{-2} under an applied electric field of 1000 V cm^{-1}. The DPSI device showed a dark current drift of 5.6×10^{-7} nA cm^{-1} V^{-1} s^{-1}, a reduction of approximately 84% compared to the pristine device (3.5×10^{-6} nA cm^{-1} V^{-1} s^{-1}). These results confirm that the DPSI-based device shows a more controlled dark current due to reduced trap density.

3.2 Strain in $FAPbBr_3$ single crystals

The internal bulk strain of the DPSI-based SCs was then investigated using polarised light microscopy (PLM). In this technique, the crystal is placed between a pair of crossed polarising mirrors, illuminated from below by light from a light-emitting diode (LED) source. When the polarisers are oriented at 90° to each other, strain-induced birefringence within the crystal becomes clearly visible, where the strained regions appear bright under the microscope, while the unstrained regions remain dark. The PLM image of a DPSI-based single crystal is shown in Fig. 4a.

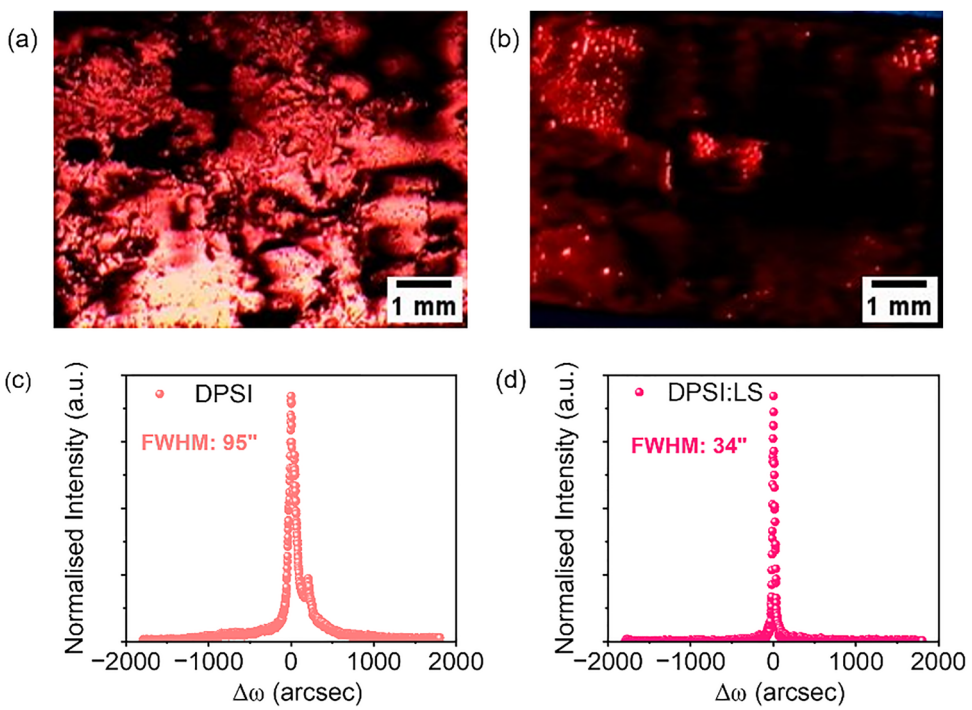

Fig. 4 (a) PLM image of the DPSI SC. (b) PLM image of the DPSI:LS SC. (c) High-resolution (100) X-ray rocking curve (XRRC) of the DPSI-based SC. (d) XRRC for the DPSI:LS SC.

Under polarised light, the DPSI-based SC shows a significant amount of illuminated regions, indicating that the SC is significantly strained. Whilst DPSI helps in the regulation of the crystal growth process, there is no direct evidence from the PLM images that the bulk strain of the SCs is significantly improved. Bulk strain causes defects in perovskite SCs and impedes charge transport.[12] Previous work showed that temperature fluctuations during the initial stages of the crystal growth induce a strain towards the seed crystal, which then propagates through the crystal growth process.[10] A modified temperature ramp was therefore used, initiating the growth process at room temperature (25 °C). This tended to reduce the temperature inhomogeneity between the seed and the growth solution (see Fig. S3b for the final optimised temperature ramp). Using this modified temperature ramp, low-strained FPB SCs (henceforth referred to as DPSI:LS) were grown, as shown in Fig. 4b.

We also carried out cross-polarised Raman spectroscopic measurements on both strained DPSI and DPSI:LS FPB SCs. Polarised Raman spectroscopy is a useful technique that provides information regarding the vibrational modes, molecular structure and symmetry of well-ordered materials such as crystals, polymers and carbon materials. This technique can facilitate the determination of anisotropy, molecular orientation, extent of amorphicity and crystallinity and allows the characterisation of strain/stress in materials.[25–27]

Polarised Raman spectra of both DPSI and DPSI:LS FPB SCs show a broad peak with a peak maximum at 120 cm^{-1}, which corresponds to the ν_s (symmetric stretching vibration) of the Br–Pb–Br bond[28,29] (see Fig. S4). It was observed that the intensity of the Raman peak that corresponds to the Br–Pb–Br stretching peak is higher in the strained FPB SC compared to the low-strained FPB SC. This is consistent with the observations in other perovskites such as MPB and $FAPbI_3$ SCs, where strain in the perovskite lattices increases the Raman peak intensity. This originates from strain-induced lattice distortions in the perovskite crystal structure.[30,31] We also conducted cross-polarised Raman spectroscopic mapping, where the intensity of the peak centred at 120 cm^{-1} was mapped over the surface of the single crystal. The Raman map directly corresponded to the observations from the PLM images of DPSI and DPSI:LS single crystals, as shown in Fig. S5. This indicates that both PLM and cross-polarised Raman spectroscopy independently verify the presence of strain in DPSI FPB SCs and a reduction of strain in the DPSI:LS FPB SCs.

We further carried out high-resolution X-ray rocking curve (XRRC) measurements of the (100) phase of FPB SCs grown using the two different heat ramps. The XRRC of the strained single crystal shows a broad FWHM of 95 arc seconds (0.0264°) and multiple features, as shown in Fig. 4c. The multiple features on the XRRC are due to misoriented domains and low angle boundaries.[32] It is known that misoriented domains cause strain in perovskites.[33] Considering the DPSI:LS SCs, the XRRC is significantly narrower, and was calculated to be 34 arc seconds (0.0094°) (Fig. 4d). The narrower FWHM indicates a significant improvement in the crystallinity of the FPB SCs grown using the modified temperature ramp. The (100) XRRC of the DPSI:LS SC does not show multiple peaks, which indicates a reduction of the misoriented domains and low angle boundaries, which would result in a lower strained SC. The combined observations from PLM, cross-polarised Raman spectroscopy, and XRRCs of the DPSI:LS SCs indicate a consistent reduction in lattice distortion and crystallographic misorientation. Therefore, this observation confirms the improvement in crystalline coherence, reduced internal disorder and strain of the FPB SCs grown using the room-temperature-initiated heat ramp.

3.3 Charge transport due to strain in $FAPbBr_3$ single crystals

Following the optimisation of the crystal growth process, we investigated how the bulk strain affects the performance of perovskite photon counting detectors, particularly through its impact on charge transport. To evaluate the charge transport dynamics of our FPB SC devices, we conducted α-particle spectroscopy using a ^{241}Am source emitting 5.49 MeV α-particles. Due to their limited penetration depth in FPB (~20–30 μm), as confirmed by stopping and range of ions in matter (SRIM) simulations (Fig. S7), α-particles serve as an ideal method for evaluating the charge transport dynamics of the crystal. In contrast to X-rays or γ-rays, which generate charge carriers throughout the bulk of the crystal, the short penetration depth only causes signal generation and charge transport from a single charge carrier type, depending on the polarity of the irradiated contact.[34] The pulse height spectrum of the DPSI-based device for 5.49 MeV α-particles operating under an electric field of 300 V cm^{-1} is shown in Fig. 5a.

Notably, the pulse height spectra of the DPSI FPB SC device show a pronounced high energy tail (HET) following the main photopeak. A similar feature was observed for melt-grown $CsPbBr_3$ SCs, suggesting that the presence of the HET may be an inherent feature of lead halide perovskite materials.[35] To gain further insight into the origins of this phenomenon, we analysed the preamplifier pulse shapes at an applied electric field of 300 V cm^{-1}. Preamplifier pulses associated with the HET showed a distinctive dual-rise time shape, comprising a fast rise and a slow rise component. Rise time analysis revealed a rapid component with a rise time of 3.2 μs and a delayed component with a significantly longer rise time of 13.3 μs, as shown in Fig. 5b. The delayed charge transport observed in the slow pulses suggests either a non-uniform mobility or an electric field within the bulk of the perovskite SC. In contrast, the preamplifier pulses contributing to the main alpha peak, as shown in Fig. 5c, only show a prompt rise time of 4.2 μs. Previous reports of the time-of-flight (TOF) analysis of MPB SCs show a similar behaviour in the current transients of strained crystals, indicating that strained perovskite devices show non-uniform charge transport, irrespective of the perovskite composition.[10]

In our low-strained DPSI:LS device, a well-resolved peak was obtained when biased at an electric field of ~300 V cm^{-1}, as shown in Fig. 5d. Analysis of the preamplifier pulses reveals a rise time of 2.7 μs (Fig. 5e), indicating faster charge collection

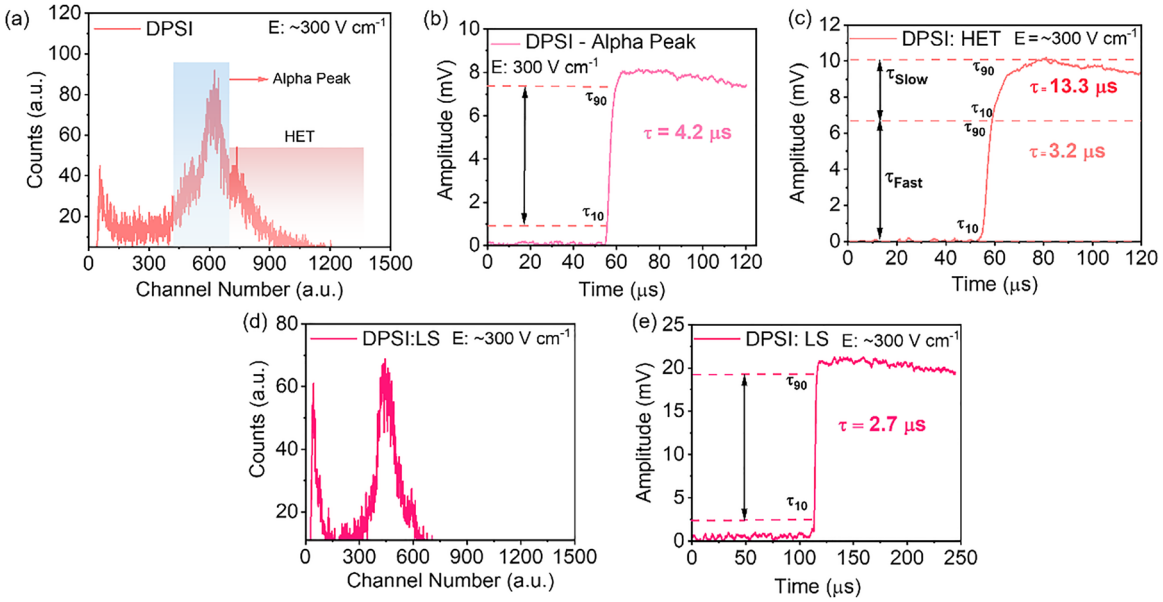

Fig. 5 (a) Pulse height spectrum of the ^{241}Am 5.49 MeV α-particles obtained from a strained DPSI-based SC under an electric field of 300 V cm^{-1}. (b) Energy spectrum generated directly from the preamplifier pulses for a DPSI-based SC device under an electric field of 300 V cm^{-1}. (c) Preamplifier pulse obtained from the high energy tail (HET) section of the energy spectrum. (d) Energy spectrum obtained for a DPSI:LS device generated directly from preamplifier pulses at 300 V cm^{-1}. (e) Preamplifier pulse obtained at 300 V cm^{-1} for a DPSI:LS device with a rise time of 2.7 μs.

in the DPSI:LS SC. These findings indicate that the bulk strain significantly affects the charge transport dynamics of perovskite SCs and reducing strain through controlled ITC growth improves the charge transport properties of perovskite photon counting detectors.

3.4 Radiation detection performance of $FAPbBr_3$ single crystal devices

We assessed the X-ray photocurrent sensitivity of the DPSI:LS FPB SC devices using a 50 kV X-ray source. The devices were irradiated at a dose rate of 878 μGy$_{air}$ s^{-1} with an applied electric field of 1000 V cm^{-1}. Fig. 6a compares the temporal X-ray photocurrent responses of the DPSI and DPSI:LS devices under an applied electric field of 1000 V cm^{-1}. The net photocurrent of the DPSI:LS device was observed to be approximately 45% higher than that of the DPSI device. We then calculated the X-ray sensitivities of these devices using

$$S = \frac{I_{\text{X-ray}} - I_{\text{dark}}}{AD} \quad (5)$$

where S is the X-ray sensitivity, $I_{\text{X-ray}}$ is the X-ray photocurrent, I_{dark} is the dark current of the detector, A is the active area of the detector (0.09 cm^{-2}) and D is the dose rate incident on the detector. Fig. 6b presents the X-ray sensitivities of the DPSI and DPSI:LS devices at an applied electric field of 1000 V cm^{-1}. The DPSI:LS device showed an excellent X-ray sensitivity of 5111 μC Gy$_{air}^{-1}$ cm^{-2}, which is approximately a 20% increase compared to the DPSI device (4245 μC Gy$_{air}^{-1}$ cm^{-2}). This X-ray sensitivity is more than two orders of magnitude higher than that of the commercially available a-Se detectors (20 μC Gy$_{air}^{-1}$ cm^{-2}).[2]

Apart from the X-ray sensitivity of these devices, other important factors are the operational and storage stability. The performance of perovskite detectors operating under high electric fields, for instance, 1000 V cm^{-1}, has been shown to deteriorate over time due to the combined effects of ion migration and electrochemical reactions of the metal contact with the perovskite. These effects will cause the dark current of the device to increase or fluctuate, reducing the signal-to-noise ratio (SNR) of the detector.[36] As shown in Fig. 6c, the fresh DPSI:LS device shows a stable photocurrent response with a very low photocurrent drift of 1.39 × 10^{-6} nA cm^{-1} s^{-1} V^{-1}. The excellent photocurrent stability of the DPSI:LS detectors is attributed to the reduced ion migration and the low dark current in the DPSI:LS device (~31 nA cm^{-2}), as shown in Fig. S6b. The long-term stability of the DPSI:LS device was investigated after being stored in the dark under a N_2 atmosphere for 2 months. Notably, the device dark current reduced, while the X-ray response of the detector remained unchanged. This phenomenon was also observed in CPB SC detectors.[37]

The limit of detection (LOD) of the devices was measured using the setup shown in Fig. S8a. According to the IUPAC standards, the LOD is defined as the dose rate at which SNR = 3.[38] By using the X-ray photocurrent method, we measured the temporal response of a DPSI:LS detector when exposed to X-ray dose rates ranging from 36.5 nGy$_{air}$ s^{-1} to 219 nGy$_{air}$ s^{-1}, as shown in Fig. S8b. The LOD of the low-strained detector was found to be 3.5 nGy$_{air}$ s^{-1}, as shown in Fig. 6(d). This LOD is approximately three orders of magnitude lower than the current dose rate used in the medical industry (5.5 μGy$_{air}$ s^{-1}), and it is also one of the lowest LODs reported for $FAPbBr_3$ SC X-ray detectors.[2,39,40]

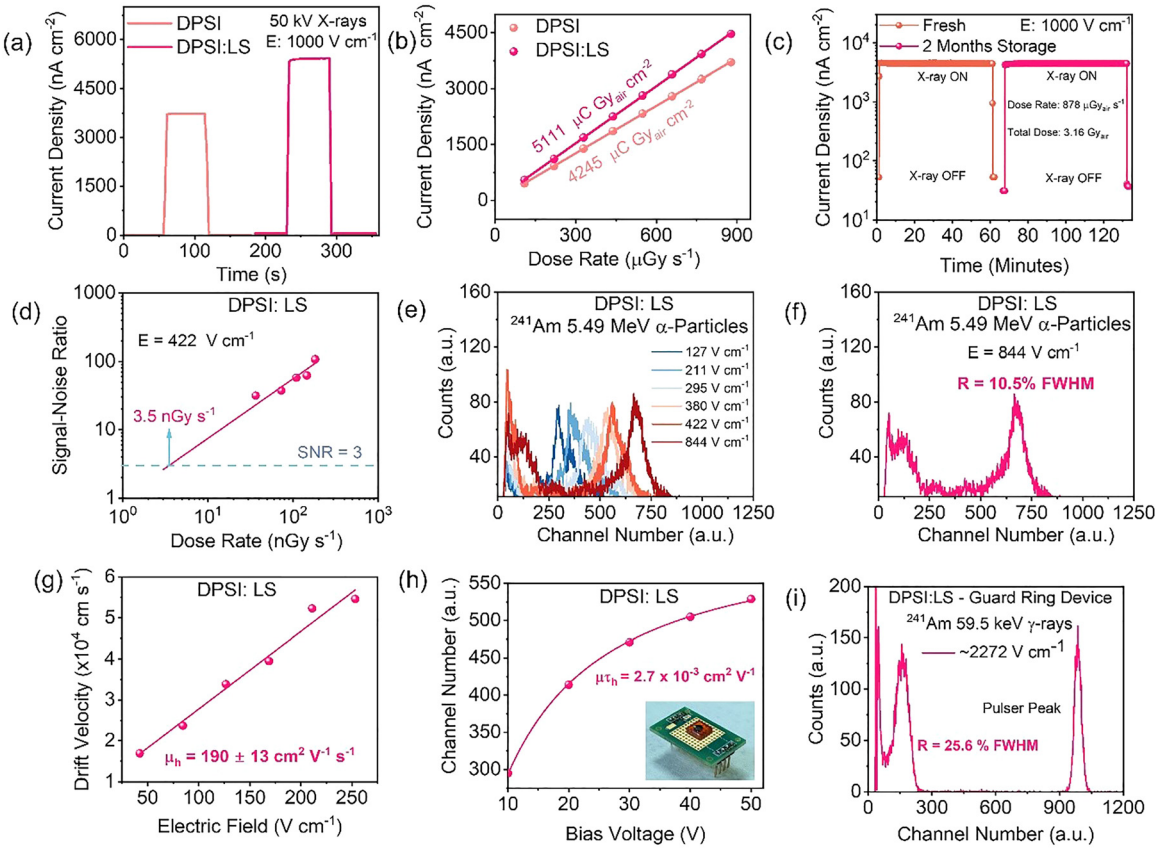

Fig. 6 (a) Temporal X-ray photocurrent response of the DPSI and DPSI:LS devices at 1000 V cm^{-1} for a 50 kV X-ray at a dose rate of 878 μGy s^{-1}. (b) X-ray sensitivity of the DPSI and DPSI:LS devices at an electric field of 1000 V cm^{-1}. (c) X-ray photocurrent stability of fresh DPSI:LS and the storage stability of the DPSI:LS device for a 50 kV X-ray at a dose rate of 878 μGy s^{-1}. (d) Limit of detection (LOD) of a DPSI:LS device at an electric field of 422 V cm^{-1}. (e) ^{241}Am 5.49 MeV α-particle pulse height spectra for different applied electric fields obtained from a DPSI:LS device. (f) ^{241}Am 5.49 MeV α-particle pulse height spectrum obtained at 844 V cm^{-1} from the DPSI:LS device. (g) Drift hole mobility of the DPSI:LS device obtained from α-particles. (h) Hole mobility–lifetime ($\mu\tau$) product of the DPSI:LS device obtained from α-particles. (i) ^{241}Am 59.5 keV γ-ray spectrum obtained from a DPSI:LS guard ring device.

The spectroscopic radiation detection performance of the DPSI:LS devices was evaluated using ^{241}Am α-particles. The pulse height spectra of the DPSI:LS device under different applied electric fields are shown in Fig. 6e. The best energy resolution obtained for the 5.49 MeV α-particles was ~10.5% FWHM at an electric field strength of ~844 V cm^{-1} (200 V bias) as shown in Fig. 6f. The device also demonstrated good operational stability under a constant high field strength of ~422 V cm^{-1} (100 V bias), showing stable alpha-particle spectra after 1 hour of continuous operation (Fig. S9a). The peak channel position stabilised after 15 minutes, likely due to the settling of the dark current (Fig. S9b). This excellent device stability is also attributed to the suppressed ion migration, as evidenced by the device maintaining low and stable dark currents even under high electric field strengths (1000 V cm^{-1}), as shown in Fig. S6b.

The drift hole mobility of the DPSI:LS device was calculated using the time-of-flight (TOF) method:[41]

$$\mu = \frac{V_{dr}}{E} = \frac{d^2}{V \times t_{dr}} \quad (6)$$

where μ is the mobility, V_{dr} is the drift velocity, E is the applied electric field, d is the thickness of the detector, V is the applied voltage and t_{dr} is the drift transit time. The hole drift mobility of the DPSI:LS device was calculated to be 190 ± 13 cm^2 V^{-1} s^{-1}, as shown in Fig. 6g. This is a 25% improvement in mobility compared to the DPSI device (151 ± 12 cm^2 V^{-1} s^{-1}), as shown in Fig. S10a.

The hole mobility–lifetime product ($\mu\tau_h$) of the detector was calculated using the single carrier Hecht equation:

$$\eta = A\frac{\mu\tau V}{d^2}\left(1 - e^{\left(\frac{-d^2}{\mu\tau V}\right)}\right) \quad (7)$$

where η is the charge collection efficiency and A is a scaling factor based on charge calibration. The $\mu\tau_h$ value was calculated to be 2.7 × 10^{-3} cm^2 V^{-1}, as shown in Fig. 6h. The $\mu\tau_h$ for the DPSI device was found to be 1.3 × 10^{-3} cm^2 V^{-1}, as shown in Fig. S10b. The $\mu\tau$ values of both DPSI and DPSI:LS FPB SC devices are in good agreement with the reported $\mu\tau$ values for FPB SC devices.[9,34,40] The electron charge transport in DPSI-based FPB devices was also investigated by recording

alpha-particle pulse height spectra under opposite bias polarity and calculating $\mu\tau_e$, as shown in Fig. S11a and b. The $\mu\tau_e$ value was found to be 7.2×10^{-4} cm^2 V^{-1}, confirming better hole transport in these materials.[9]

The performance of the low-strained DPSI:LS devices was investigated for spectroscopic γ-ray detection. One of the main criteria that needs to be satisfied for γ-ray detection is very low and stable dark currents to achieve good signal-to-noise, especially when detecting lower energy photons such as 59.5 keV gamma rays from ^{241}Am. Therefore, a guard ring contact structure was used, which suppressed the dark current of DPSI:LS devices (Fig. S6a). The DPSI:LS guard ring device achieved an ultra-low dark current of 2.9 nA cm^{-2} under an electric field of 1000 V cm^{-1} (Fig. S6b). A well-resolved full-energy peak was observed from ^{241}Am 59.5 keV γ-rays with an energy resolution of 25.6% FWHM at an applied electric field of 2272 V cm^{-1}, as shown in Fig. 6i.

To further investigate the measured energy resolution for ^{241}Am γ-rays, we characterised the electronic noise performance of our readout system and detector using an electronic pulser to inject a fixed-amplitude charge pulse into the preamplifier. The resulting pulser peak in the pulse height spectrum provides a direct measure of the intrinsic electronic noise of the measurement signal, irrespective of the charge transport processes in the detector. As shown in Fig. S12, the pulser peak shows a FWHM of ∼28 channels at 0 V cm^{-1} equivalent to ∼9 keV FWHM. The FWHM of the pulser peak does not significantly broaden even at high electric fields (∼2500 V cm^{-1}), indicating that the electronic noise is not the dominant factor that contributes to the peak broadening of the measured ^{241}Am 59.5 keV gamma peak. Therefore, we attribute the relatively broad width of the 59.5 keV photopeak (26.6% FWHM, ∼16 keV FWHM) to charge transport non-uniformities across the surface area of the crystal. The performance statistics of multiple DPSI:LS devices are shown in Table S1. A comparison of the current performance of perovskite photon counting detectors is shown in Table S2.

4. Conclusions

In this work, we have demonstrated that the use of the DPSI ligand effectively addresses issues in the growth of FPB SCs, such as spontaneous nucleation, unregulated crystal growth kinetics, and limitations in obtaining scalable crystals. Furthermore, we optimized the crystal growth temperature ramp, which significantly reduced the bulk strain of our DPSI-based FPB SCs. Through these modifications, we have managed to obtain high-quality FPB SCs, evidenced by the (100) XRRC FWHM of 34 arc seconds, showing high levels of crystallinity in the DPSI:LS SCs. Examination of the effect of strain on the charge transport dynamics revealed that bulk strain is detrimental to efficient charge transport in perovskite SCs. The DPSI:LS SC photon counting detector exhibited an excellent μ_h of 190 cm^2 V^{-1} s^{-1}, a high $\mu\tau_h$ of 2.7×10^{-3} cm^2 V^{-1} and an ultra-low dark current of ∼3 nA cm^{-2} at an applied electric field of 1000 V cm^{-1} with the use of a guard ring contact structure. The DPSI:LS device resolved ^{241}Am 5.49 MeV α-particles with a 10.5% FWHM energy resolution and ^{241}Am 59.5 keV γ-rays with an energy resolution of 25.6% FWHM, and achieved a high X-ray sensitivity of 5111 μC Gy_{air}^{-1} cm^{-2} along with a LOD of 3.5 nGy_{air} s^{-1}. These results highlight the strong potential of FPB SCs as next-generation room-temperature semiconductor radiation detectors that can efficiently operate in both current and photon-counting modes.

Conflicts of interest

There are no conflicts of interest.

Data availability

The data supporting this article have been included as part of the supplementary information (SI). Supplementary information is available. See DOI: https://doi.org/10.1039/d5tc03740a.

Acknowledgements

J.J. and P.S. acknowledge funding from the Defence Threat Reduction Agency (DTRA) through the IIRM University Research Alliance under award no. HDTRA1-20-2-0002. Fig. 1(a) was created in BioRender. Jayarathne, J. (2025) https://BioRender.com/gkl1t4d. The TOC figure was created in BioRender. Jayarathne, J. (2026) https://BioRender.com/vaweg5w. The authors thank Dr Rachida Bance-Soualhi for assistance with the FTIR measurements.

References

1 P. J. Sellin, *Nucl. Instrum. Methods Phys. Res., Sect. A*, 2003, **513**, 332–339.
2 S. O. Kasap, *J. Phys. D: Appl. Phys.*, 2000, **33**, 2853–2865.
3 J. Eberth and J. Simpson, *Prog. Part. Nucl. Phys.*, 2008, **60**, 283–337.
4 S. Tokuda, H. Kishihara, S. Adachi and T. Sato, *J. Mater. Sci.: Mater. Electron.*, 2004, **15**, 1–8.
5 Z. Chen, Y. Zhu and Z. He, *Nucl. Instrum. Methods Phys. Res., Sect. A*, 2020, **980**, 164501.
6 F. Liu, R. Wu, Y. Zeng, J. Wei, H. Li, L. Manna and A. D. Mohite, *Nanoscale*, 2022, **14**, 6743–6760.
7 Y. He, M. Petryk, Z. Liu, D. G. Chica, I. Hadar, C. Leak, W. Ke, I. Spanopoulos, W. Lin, D. Y. Chung, B. W. Wessels, Z. He and M. G. Kanatzidis, *Nat. Photonics*, 2021, **15**, 36–42.
8 Y. He, L. Matei, H. J. Jung, K. M. McCall, M. Chen, C. C. Stoumpos, Z. Liu, J. A. Peters, D. Y. Chung, B. W. Wessels, M. R. Wasielewski, V. P. Dravid, A. Burger and M. G. Kanatzidis, *Nat. Commun.*, 2018, **9**, 1–8.
9 X. Liu, M. Xu, Y. Hao, J. Fu, F. Wang, B. Zhang, S. Bennett, P. Sellin, W. Jie and Y. Xu, *ACS Appl. Mater. Interfaces*, 2021, **13**, 15383–15390.
10 Y. Li, H. Tian, N. Li, J. Guo, X. Ling, J. Yuan, J. Zhao and Y. Deng, *Cryst. Growth Des.*, 2024, **24**, 4473–4480.

11 S. Amari, J. M. Verilhac, E. Gros D'Aillon, A. Ibanez and J. Zaccaro, *Cryst. Growth Des.*, 2020, **20**, 1665–1672.
12 F. Yu, Y. Song, L. Wang, Y. Yang, J. Wang, X. Shen, B. Jin, H. Song, Y. Fang and Q. Dong, *Small*, 2025, **21**, 1–8.
13 L. Zhao, Y. Zhou, Z. Shi, Z. Ni, M. Wang, Y. Liu and J. Huang, *Nat. Photonics*, 2023, **17**, 315–323.
14 Y. Liu, X. Zheng, Y. Fang, Y. Zhou, Z. Ni, X. Xiao, S. Chen and J. Huang, *Nat. Commun.*, 2021, **12**, 4–11.
15 M. Li, S. Wang, A. Wood, J. D. Yeager, S. P. Stepanoff, J. C. Adler, Z. Shi, J. Wang, Z. Li, D. E. Wolfe and J. Huang, *Nat. Mater.*, 2025, **24**, 1993–2000.
16 A. Franz, D. M. Többens, F. Lehmann, M. Kärgell and S. Schorr, *Acta Crystallogr., Sect. B:Struct. Sci., Cryst. Eng. Mater.*, 2020, **76**, 267–274.
17 M. E. Liao, K. Huynh, L. Matto, D. P. Luccioni and M. S. Goorsky, *J. Vac. Sci. Technol., A*, 2023, **41**, 013205.
18 R. M. Lavelle, W. J. Everson, D. J. Erdely, L. A. M. Lyle, S. W. Pistner, S. R. Hallacher, J. M. Redwing and D. W. Snyder, *Mater. Sci. Semicond. Process.*, 2025, **190**, 109341.
19 X. Zheng, Y. Deng, B. Chen, H. Wei, X. Xiao, Y. Fang, Y. Lin, Z. Yu, Y. Liu, Q. Wang and J. Huang, *Adv. Mater.*, 2018, **30**, 1–8.
20 J. Zhang, X. Xing, D. Qian, A. Wang, L. Gu, Z. Kuang, J. Wang, H. Zhang, K. Wen, W. Xu, M. Niu, X. Du, L. Yuan, C. Cao, Y. Cao, L. Zhu, N. Wang, C. Yi, W. Huang and J. Wang, *Adv. Funct. Mater.*, 2022, **32**, 1–7.
21 J. W. Kleppinger, S. K. Chaudhuri, O. F. Karadavut, R. Nag and K. C. Mandal, *J. Cryst. Growth*, 2022, **583**, 126532.
22 V. M. Le Corre, E. A. Duijnstee, O. El Tambouli, J. M. Ball, H. J. Snaith, J. Lim and L. J. A. Koster, *ACS Energy Lett.*, 2021, **6**, 1087–1094.
23 Y. Liu, B. J. Kim, H. Wu, G. Boschloo and E. M. J. Johansson, *ACS Appl. Energy Mater.*, 2021, **4**, 9276–9282.
24 M. Xia, J. H. Yuan, G. Niu, X. Du, L. Yin, W. Pan, J. Luo, Z. Li, H. Zhao, K. H. Xue, X. Miao and J. Tang, *Adv. Funct. Mater.*, 2020, **30**, 2–9.
25 G. Reuveni, Y. Diskin-Posner, C. Gehrmann, S. Godse, G. G. Gkikas, I. Buchine, S. Aharon, R. Korobko, C. C. Stoumpos, D. A. Egger and O. Yaffe, *J. Phys. Chem. Lett.*, 2023, **14**, 1288–1293.
26 S. Wood, G. P. Rigas, A. Zoladek-Lemanczyk, J. C. Blakesley, S. Georgakopoulos, M. Mas-Torrent, M. Shkunov and F. A. Castro, *Sci. Rep.*, 2016, **6**, 1–8.
27 R. Ossikovski, G. Picardi, G. Ndong and M. Chaigneau, *C. R. Phys.*, 2012, **13**, 837–852.
28 F. H. Naqvi and J. H. Ko, *J. Raman Spectrosc.*, 2023, **54**, 1138–1149.
29 G. Reuveni, Y. Diskin-Posner, C. Gehrmann, S. Godse, G. G. Gkikas, I. Buchine, S. Aharon, R. Korobko, C. C. Stoumpos, D. A. Egger and O. Yaffe, *J. Phys. Chem. Lett.*, 2023, **14**, 1288–1293.
30 Y. Li, H. Tian, N. Li, J. Guo, X. Ling, J. Yuan, J. Zhao and Y. Deng, *Cryst. Growth Des.*, 2024, **24**, 4473–4480.
31 Y. Chen, Y. Lei, Y. Li, Y. Yu, J. Cai, M. H. Chiu, R. Rao, Y. Gu, C. Wang, W. Choi, H. Hu, C. Wang, Y. Li, J. Song, J. Zhang, B. Qi, M. Lin, Z. Zhang, A. E. Islam, B. Maruyama, S. Dayeh, L. J. Li, K. Yang, Y. H. Lo and S. Xu, *Nature*, 2020, **577**, 209–215.
32 N. P. Jasti, I. Levine, Y. (Isai) Feldman, G. Hodes, S. Aharon and D. Cahen, *Proc. Natl. Acad. Sci. U. S. A.*, 2024, **121**, 2017.
33 S. Jariwala, H. Sun, G. W. P. Adhyaksa, A. Lof, L. A. Muscarella, B. Ehrler, E. C. Garnett and D. S. Ginger, *Joule*, 2019, **3**, 3048–3060.
34 S. H. Bennett, J. Ghosh, E. Gros-Daillon, F. Lédée, J. Mayén Guillén, J.-M. Verilhac, J. Zaccaro, D. Y. Chung, V. Klepov, M. G. Kanatzidis and P. J. Sellin, *Front. Detect. Sci. Technol.*, 2023, **1**, 1–12.
35 Y. He, Z. Liu, K. M. McCall, W. Lin, D. Y. Chung, B. W. Wessels and M. G. Kanatzidis, *Nucl. Instrum. Methods Phys. Res., Sect. A*, 2019, **922**, 217–221.
36 Y. Wu, J. Feng, Z. Yang, Y. Liu and S. Liu, *Adv. Sci.*, 2023, **10**, 1–48.
37 N. Shen, X. He, T. Gao, B. Xiao, Y. Wang, R. Ren, H. Qin, K. S. Bayikadi, Z. Liu, J. A. Peters, B. W. Wessels, L. Wang, X. Ouyang, S. Wei, Q. Sun, X. Liu, Y. Lai, X. Ouyang, Z. Chai, M. G. Kanatzidis and Y. He, *Nat. Commun.*, 2025, **16**, 8113.
38 M. Sytnyk, S. Deumel, S. F. Tedde, G. J. Matt and W. Heiss, *Appl. Phys. Lett.*, 2019, **115**, 190501.
39 W. Jiang, H. Li, Z. Xing, Y. Zhao, D. Liu, H. Di, C. Zhao, Y. Liu and Y. Zhao, *ACS Appl. Mater. Interfaces*, 2024, **16**, 51630–51638.
40 W. Jiang, J. Ren, H. Li, D. Liu, L. Yang, Y. Xiong and Y. Zhao, *Small Methods*, 2023, **7**, 1–8.
41 P. J. Sellin, A. W. Dazvies, A. Lohstroh, M. E. Özsan and J. Parkin, *IEEE Trans. Nucl. Sci.*, 2005, **52**, 3074–3078.
42 Y. He, W. Ke, G. C. B. Alexander, K. M. McCall, D. G. Chica, Z. Liu, I. Hadar, C. C. Stoumpos, B. W. Wessels and M. G. Kanatzidis, *ACS Photonics*, 2018, **5**, 4132–4138.
43 X. Liu, Q. Zhang, D. Zhao, R. Bai, Y. Ruan, B. Zhang, F. Li, M. Zhu, W. Jie and Y. Xu, *ACS Appl. Mater. Interfaces*, 2022, **14**, 51130–51136.
44 R. Wu, Y. Yue, Q. Wang, J. Wei, L. Manna, F. Liu and H. Li, *ACS Appl. Mater. Interfaces*, 2025, **17**, 8055–8063.
45 T. Wang, X. Zhang, Q. Zhang, X. Liu, H. Luo, Y. Hao, R. Bai, L. Xu, J. Liu and Y. Xu, *ACS Photonics*, 2024, **11**, 4707–4715.
46 X. Zhang, R. Bai, Y. Fu, Y. Hao, X. Peng, J. Wang, B. Ge, J. Liu, Y. Hu, X. Ouyang, W. Jie and Y. Xu, *Nat. Commun.*, 2024, **15**, 6333.
47 Q. Zhang, X. Liu, X. Zhang, Z. Wang, B. Zhang, Y. Hao, A. Dubois, W. Jie and Y. Xu, *J. Mater. Chem. A*, 2023, **12**, 3304–3310.